

# Comparative Evaluation of Tracking Capability of Spatial Patterns on Defective Urban Solar Panels between Unmanned Aerial Vehicle Video Stream and Photomosaics

Young-Seok Hwang,<sup>1</sup> Jung-Sup Um,<sup>2</sup> and Jun-Hyun Kim<sup>2\*</sup>

<sup>1</sup>Korea Environment Institute, Sicheong-daero 370, Sejong 30147, South Korea

<sup>2</sup>Department of Geography, Kyungpook National University,  
University Road 80, Buk-gu, Daegu 41566, South Korea

(Received June 25, 2022; accepted September 22, 2022)

**Keywords:** unmanned aerial vehicle (UAV), video, solar panel, photomosaic, thermal deficiency, hot spots, clustering

Unmanned aerial vehicle (UAV) autopilot flight requires a specific altitude when inspecting defective urban solar panels to avoid obstacles such as high-rise buildings, trees, and telegraph poles. Therefore, autopilot-based thermal imaging has severe data redundancy because the non-solar panel area occupies more than 99% of the ground target. We aim to explore the tracking capability of a UAV video stream for defective urban solar panels by comparing spatial and clustering patterns with autopilot-based photomosaics. The spatial patterns of distributions and clusters in defective solar panels have high similarity (80–100%) to those of autopilot-based photomosaics. The results of this study can serve as a valuable reference for video-stream-based thermal deficiency inspections of defective solar panels in urban areas.

## 1. Introduction

A solar panel defect can be broadly defined as any abnormality on the panel. Common defects include mismatch, cracks, discolorations, snail trails/tracks, and soiling.<sup>(1,2)</sup> These defects can decrease the power generation efficiency of solar modules. Solar panels convert photons into electricity by exciting electrons in the atoms of a semiconductor material. The energized electrons then generate an electric voltage and current, and the former is transmitted to the inverter. If the solar panels are short-circuited or malfunctioning, abnormal heat generation due to overloading occurs. This heat is manifested as thermal hot spots—also known as thermal deficiency—on the solar panels. Accordingly, thermal imaging is commonly utilized to detect defective solar panels by identifying the thermal deficiency.

Autopilot-based thermal imaging using still images is now a standard procedure, replacing in situ visual inspection and  $I$ - $V$  curve tests because of its shorter time and higher cost efficiency.<sup>(3,4)</sup> Autopilot flight is conducted along predefined waypoints following a specific flight plan for the target area. Typically, urban solar panels are scattered and account for only 1%

---

\*Corresponding author: e-mail: [kamcho78@knu.ac.kr](mailto:kamcho78@knu.ac.kr)  
<https://doi.org/10.18494/SAM3999>

of the total roof area in a city. Urban solar panels only take up 10% of the rooftop surface in a standard single-family house with six or fewer panels (1 m width and 1.6 m height).<sup>(5)</sup> The target area covered by autopilot flight may be at least several hundred square meters (for example,  $30 \times 30 = 900 \text{ m}^2$ ). The possible keypoints are obtained from less than four predefined waypoints.<sup>(6)</sup> Additionally, autopilot flight in an urban area must be at an altitude that avoids obstacles, such as high-rise buildings, trees, and telegraph poles, increasing the difficulty of securing sufficient keypoints.

Thus, autopilot-based thermal imaging has severe data redundancy, with the area not covered by solar panels occupying more than 99% of the ground target. This causes a shortfall of thermal markers on solar panels, resulting in matching failure or mismatch on a single solar panel during the construction of thermal photomosaics. Data redundancy may cause errors in exterior orientation parameters, such as direct distance measurements, angles, positions, and solar panel areas.<sup>(7)</sup> Furthermore, unnecessary targets may contaminate the thermal signatures from solar panels through the influence of their ambient light.<sup>(7,8)</sup> The problem of insufficient thermal markers can be solved by exclusively obtaining still images of solar panels, comprising 1% of the total roof area, with a high overlapping rate.

Video has unique properties, offering several advantages for securing sufficient and accurate keypoints for targets. Unlike the static imagery captured by autopilot flight with predefined waypoints, dynamic stereo coverage between individual frames can be accomplished via intensive overlapping within a single solar panel.<sup>(9–11)</sup> Video-based thermal imaging can capture the thermal signatures from specifically targeted objects with constant overlapping rates within the confined area.<sup>(9)</sup> This can complement the data redundancy in traditional thermal images captured during autopilot flight owing to the scattered solar panels in urban environments.

Most studies on unmanned aerial vehicle (UAV)-borne video thermal imaging have evaluated its applicability to the real-time detection, classification, and tracking of objects,<sup>(12–14)</sup> such as in the field phenotyping of water stress<sup>(15)</sup> and fire monitoring.<sup>(16)</sup> Several studies have explored real-time mosaicking for detecting defective solar panels in large-scale solar farms with UAV video thermal imaging.<sup>(17,18)</sup> For example, Lafkih and Zaz proposed a live detection technique for shaded captured frames from solar panels in UAV video frames based on the Otsu thresholding algorithm.<sup>(17)</sup> However, these studies involved capturing images containing multiple solar panels in each scene at a relatively high flight altitude to cover a wide area. The capability of UAV-borne video in tracking the defects of a scattered urban solar panel has not been evaluated. Other studies have evaluated the suitability of UAV-borne video thermal imaging in terms of mapping accuracy<sup>(5)</sup> and thermal signature<sup>(19)</sup> and compared it with the autopilot-based imaging of solar panels.<sup>(2)</sup>

However, to our knowledge, there have been no studies on comparing the tracking capability of spatial patterns on defective urban solar panels between UAV video stream and photomosaic techniques. To utilize video as a complementary tool for the thermal deficiency inspection of scattered urban solar panels, it should adequately detect the spatial patterns on defective solar panels. Therefore, we aim to compare spatial patterns of thermal anomalies from UAV video streams and photomosaics to evaluate the applicability of a video stream to the thermal deficiency inspection of urban solar panels.

## 2. Materials and Methods

### 2.1 Study area

The study area is in the southeastern part of South Korea at  $35^{\circ}50'54''$  N latitude and  $128^{\circ}32'41''$  E longitude (Fig. 1). It is in the Dalseo administrative district of the metropolitan city Daegu, the third most populous city in South Korea. Compared with other Korean cities, Daegu has low rainfall and abundant solar radiation,<sup>(20–22)</sup> making it suitable for solar power generation. The experimental target, Daegu Educational Training Institute (DETI), is in the Gamsam-dong residential area. It is characterized by districts and land mosaics, such as commercial and residential areas, schools, and parks, in the city center. Diverse tilts ( $25\text{--}88^{\circ}$ ) and azimuths ( $120^{\circ}$ ,  $240^{\circ}$ ) are evident in the solar panels installed at DETI, which are scattered across 20% of its roof area. There is a sufficient number (645) of samples (solar panels) to ensure statistical significance. Therefore, the location is suitable for a comparative evaluation of UAV video and photomosaic techniques for the thermal deficiency inspection of urban rooftop solar panels.

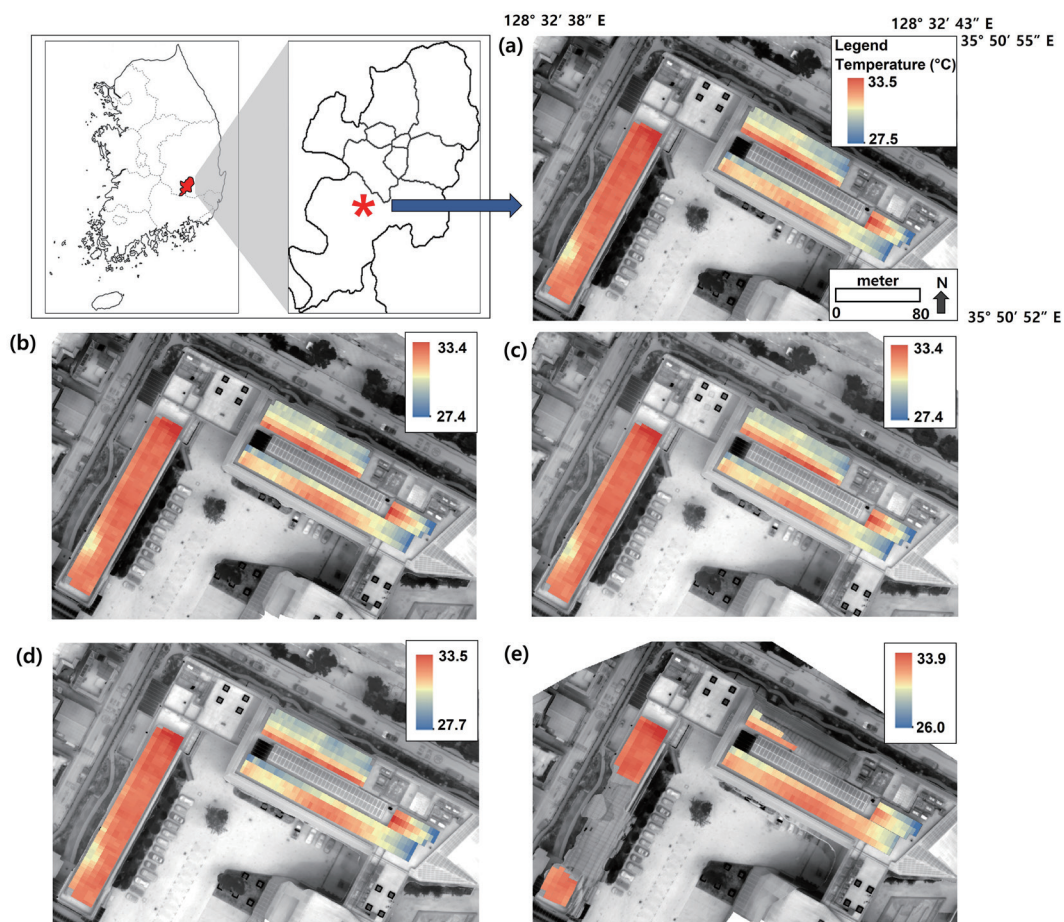


Fig. 1. (Color online) UAV thermal mosaic of experimental site processed by Pix4dMapper with images taken from autopilot and video stream: (a) autopilot, (b) 15, (c) 7.5, (d) 1, and (e) 0.5 frame/s.

## 2.2 Video-based thermal mosaic

The UAV video was recorded on 24 August 2020 (summer) when the solar zenith angle was the highest (13:00) to avoid shade and poor weather such as rainfall. The UAV thermal video of solar panels was recorded using a DJI Matrice 200 V2 quadcopter equipped with a DJI Zenmuse XT2 camera (Table 1).

In the case of the video, the CMOS sensor transmits the converted IR radiation as electrical signals into two different channels and processes a video frame image composed of two fields: (1) an odd field consisting of the thermal pixel values of odd-numbered lines and (2) an even field consisting of the thermal pixel values of even-numbered lines.<sup>(23)</sup> During this process of video frame formatting, the video frames are compressed and stored at lower spatial resolutions. Therefore, raw UAV thermal video frames do not contain geometric information. The DJI Matrice 200 V2 UAV and DJI Zenmuse XT2 camera provide telemetry data for full orientation (position and altitude) in subtitle format (SubRip Subtitle: SRT), along with the recorded thermal video. The time sync function of OSDK V3.8.1 embedded in the flight controller aligns the recording duration of the video, the GPS time, and the flight controller clock at 1 Hz. Thus, the SRT file provides second-by-second full orientation data consisting of a number indicating the sequence, Coordinated Universal Time (UTC), and all the orientation parameters (GPS coordinates, barometer altitude) acquired from the flight controller during the flight. In this study, we utilized FLIR Tools to extract thermal video imagery from the SEQ video file. The full frame rate of DJI Zenmuse XT2 is 30 Hz (30 frames/s). In this study, we built video mosaics using the extracted video frames. However, some frames were blurred due to flight vibration and the low aperture of DJI Zenmuse XT2 (F/1.0). Therefore, the frame interval per second for the UAV thermal video was chosen as 0.012 s (2 frames/s, overlap: 99%), 0.025 s (4 frames/s, overlap: 99%), 1 s (1 frame/s, overlap: 97%), and 2 s (0.5 frame/s, overlap: 88%) to reduce noise and guarantee the overlap rate. Autopilot flight was performed along a double-grid path with a 95% overlap rate. Mosaics of individual video frames and still photos were automatically created

Table 1  
Specifications of UAV and thermal camera.

UAV (DJI Matrice 200 V2)		Camera (DJI Zenmuse XT2)	
Weight	4.69 kg	Pixel numbers (width × height)	640 × 512
Maximum flight altitude (flight altitude used in this experiment: 80 m)	3000 m	Sensor size (width × height)	10.88 × 8.7 mm <sup>2</sup>
		Focal length*	19 mm
		FOV/IFOV	32° 26'/0.895 m
Hovering accuracy	<i>z</i> (height)	Vertical, ±0.1 m Horizontal, ±0.3 m	Spectral band ISO
	<i>x, y</i> (location)	Horizontal, ±1.5 or ±0.3 m (Downward Vision System)	7.5–13.5 μm 128
Maximum flight speed	61.2 km/h (P-mode)	Full frame rate	30 Hz
		Exposure value	4.55
		Sensitivity [NEDT]/ Aperture	<0.05 °C, f/1.0

\*Focal length of Zenmuse XT2 fixed at 19 mm while capturing video and still images in autopilot mode.

NEDT: Noise-equivalent differential temperature

using Pix4dMapper photogrammetry software through the following steps: (1) keypoint extraction and matching of aligned images, (2) optimization of the camera model, (3) geolocating of the GPS/ground control point (GCP) of aligned images, (4) building of point cloud and mesh (point densification and 3D textured mesh) of aligned images, and (5) building of a digital surface model (DSM), orthomosaic, and index.

Pix4dMapper utilizes the structure from motion (SfM) technique, inferring 3D information using overlapping images. This method obtains the information required to construct 3D images, such as focal length, camera type, and image size, from a set of corresponding points in two or more images. SfM photogrammetry facilitates the fast, automated, and low-cost acquisition of 3D data using a superimposed image without requiring the input of GCP information.

An SfM algorithm is applied to establish the camera exposure position and motion trajectory required to build a sparse point cloud.<sup>(24–28)</sup> The camera exposure position and motion trajectory are then used for camera calibration. Multiview stereo (MVS) is utilized to build a dense point cloud, along with the DSM generation method using reverse distance weight interpolation.<sup>(29,30)</sup> Figure 2 presents the number of overlapped images used to build the point cloud. Green areas

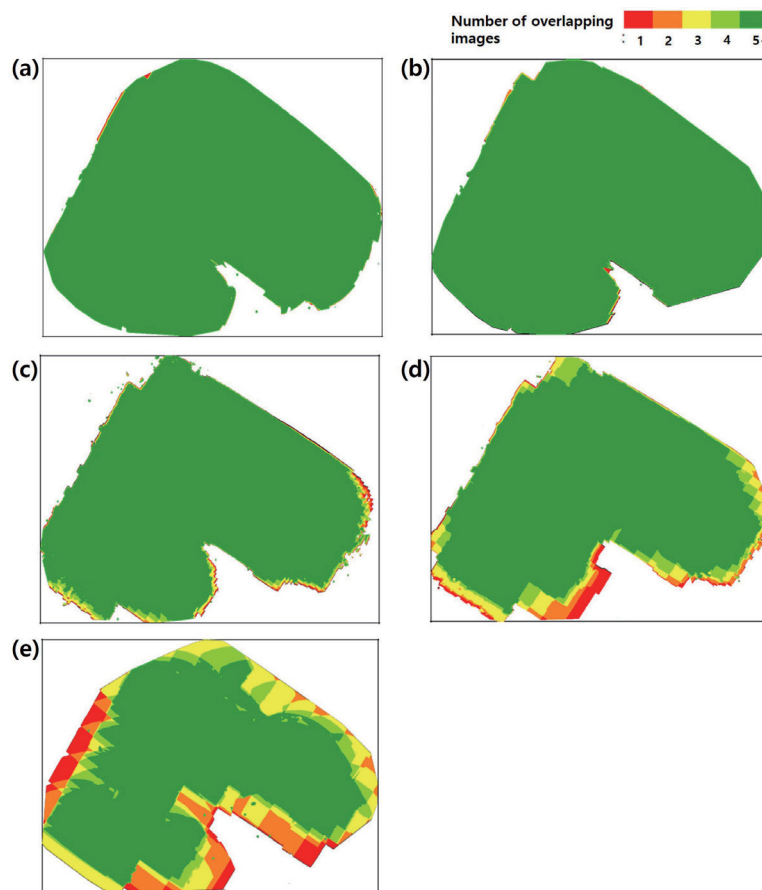


Fig. 2. (Color online) Number of overlapped images of experimental site obtained from the point cloud. Green areas indicate an overlap of at least five images. Red and yellow areas indicate a low degree of overlap, resulting in low-quality imagery: (a) photomosaic, (b) 15, (c) 7.5, (d) 1, and (e): 0.5 frame/s.

represent an overlap of at least five images for every pixel. Generally, mosaics generated from autopilot and video frames are green except for their borders. The overlap ratios, keypoints, and matched keypoints are sufficient to generate high-quality results (Fig. 2).

To acquire the land surface temperature (LST) of individual solar panels, we set and number the locations and boundaries of individual solar panels through on-screen digitization with visual interpretation. The boundary of the individual solar panels is used to identify the mean LST of the solar panels. Table 2 shows the numbers of pixels and LST values detected from the solar panel boundaries presented in Fig. 1. The numbers of solar panels obtained from the autopilot-based mosaic (hereinafter referred to as a photomosaic) and video stream (hereinafter, video mosaic) are identical for the different frame intervals (15, 7.5, and 1 frame/s). However, the numbers of pixels and solar panels in the video mosaic processed with 0.5 frame/s intervals were lower than those obtained from the photomosaic and video mosaic with shorter frame intervals (15, 7.5, and 1 frame/s) (Fig. 1). This is because of the smaller amount of overlapping imagery (88%) for 0.5 frame/s (Fig. 2). This increases the standard deviation of the LSTs in the video mosaic for 0.5 frame/s to 1.15, indicating that the distribution of LSTs of solar panels in the video mosaic for 0.5 frame/s is different from that in the photomosaic.

### 2.3 Hot-spot analysis (Getis-Ord $G_i^*$ )

Spatial autocorrelation is based on Tobler's First Law of Geography: "Everything is related to everything else, but near things are more related than distant things." Getis-Ord  $G_i^*$  is a spatial autocorrelation technique. It statistically measures the degree of spatial autocorrelation and tests the null hypothesis—the region of interest does not show any spatial pattern other than an accidental distribution.<sup>(31)</sup> We analyze the adjacent distance and patterns of the LST in malfunctioning solar panels caused by soil and dust in the photo- and video mosaics through hot-spot analysis. Then, we evaluate the distribution of the LSTs at malfunctioning solar panels to compare the spatial patterns of the LSTs in photo- and video mosaics. Herein, the Getis-Ord

Table 2  
Descriptive statistics of detected LST (°C) from solar panels in photomosaic and video mosaics.

Category	Photomosaic	15 frames/s	7.5 frames/s	1 frame/s	0.5 frame/s	
Number of pixels detected from solar panels	141767	143288	143539	146185	87340	
LST of individual solar panel pixels	Min	26.03	26.06	26.02	25.38	24.63
	Max	38.50	37.86	38.36	37.51	38.24
	Mean	31.50	31.47	31.47	31.47	31.60
	Standard deviation	0.57	0.55	0.58	0.60	0.59
Number of solar panels	645	645	645	645	359	
LST of individual solar panels	Min	27.46	27.40	27.44	27.74	26.02
	Max	33.47	33.35	33.42	33.46	33.95
	Mean	31.52	31.52	31.52	31.53	31.64
	Standard deviation	0.98	0.97	0.97	0.98	1.15
Overlapping rate	95	99	99	97	88	

$G_i^*$  statistic is calculated through the weight of the space using the LSTs. Thus, the spatial clustering can be determined from the high and low values of the calculated p-values and z-scores. The formula for calculating the Getis-Ord  $G_i^*$  statistic is<sup>(32)</sup>

$$G_i^* = \frac{\sum_{j=1}^n w_{i,j} x_j - \bar{X} \sum_{j=1}^n w_{i,j}}{\sqrt{\frac{n \sum_{j=1}^n w_{i,j}^2 - (\sum_{j=1}^n w_{i,j})^2}{n-1}}}, \quad (1)$$

$$\bar{X} = \frac{\sum_{j=1}^n x_j}{n}, \quad (2)$$

$$S = \sqrt{\frac{\sum_{j=1}^n x_j^2}{n} - (\bar{X})^2}, \quad (3)$$

where  $x_j$  is the LST for point  $j$ ,  $w_{i,j}$  is the spatial weight between points  $i$  and  $j$ , and  $n$  is the total number of LSTs. The Getis-Ord  $G_i^*$  statistic, calculated by considering the distance between points, determines statistical significance via the z-test. In other words, the clustering of high and low values of LST is determined through statistical significance by considering the concentrations of the high and low values of LSTs. If the z-score is positive (+), the high values are spatially clustered, and if the z-score is negative (−), the low values are spatially clustered.

### 3. Results and Discussion

Figure 3 and Table 3 present the results of the hot-spot analysis and high–low clustering analysis (Getis-Ord General G) of  $LST_p$  versus  $LST_{15frames}$ ,  $LST_{7.5frames}$ ,  $LST_{1frame}$ , and  $LST_{0.5frame}$ . The z-scores of high–low clustering indicate that  $LST_p$ ,  $LST_{15frame}$ ,  $LST_{7.5frames}$ ,  $LST_{1frame}$ , and  $LST_{0.5frame}$  have highly clustered patterns (2.94–5.08) with a statistically significant p-value (0.00). In other words, the high values are more concentrically clustered than the low values in this experimental site. However,  $LST_{0.5frame}$  shows less highly clustered patterns than  $LST_{15frames}$ .  $LST_{15frames}$ ,  $LST_{7.5frames}$ , and  $LST_{1frame}$  have similar resultant mean z-scores) to  $LST_p$  (hot spot: 2.27, cold spot: −2.72) in the hot spots (from 2.31 to 2.35) and cold spots (from −2.70 to −2.68) (Fig. 3, Table 3).  $LST_{0.5frame}$  has a similar mean z-score to  $LST_p$  in the hot spots but a very different value in the cold spots. Longer frame intervals produce larger differences in the resultant mean z-scores in the cold spots, indicating lower LSTs (Table 3). The video mosaics with longer frame intervals tend to underestimate the LST compared with the autopilot-based photomosaics. This tendency may result from the time lag and vignetting effects. The thermal UAV video stream is taken 20 min after the autopilot imaging is conducted along the flight plan. LST is highest at 14:00 even though the solar zenith angle is lower than that at 13:00. The solar panels remain at an elevated temperature until 14:00, at which the peak LST

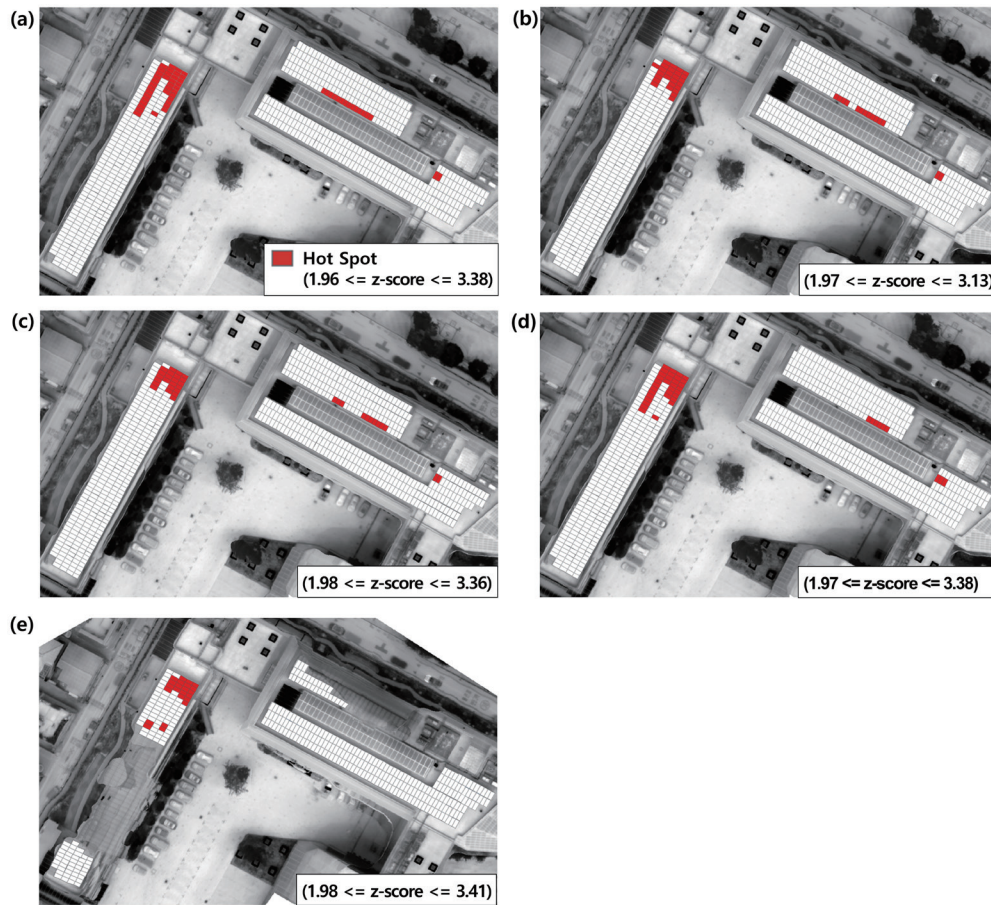


Fig. 3. (Color online) Results of hot-spot analysis (Getis-Ord Gi) of solar panels in study area: (a) photomosaic, (b) 15, (c) 7.5, (d) 1, and (e) 0.5 frame/s.

Table 3

Results of hot-spot analysis (Getis-Ord Gi) and high–low clustering analysis (Getis-Ord General G). Similarity is calculated by dividing the number of hot spots detected from the photomosaic by the number of hot spots matched between the photo- and video mosaics.

Frame interval		Photomosaic	15 frames/s	7.5 frames/s	1 frame/s	0.5 frame/s
Number of solar panels	Hot spot	53	40	35	42	23
	Spatial location similarity between photo- and video mosaics (%)	Hot spot	—	66.0	58.5	67.9
Getis-Ord Gi z-score (hot spot)	Min	1.96	1.97	1.98	1.97	1.98
	Max	3.38	3.13	3.36	3.38	3.41
	Mean	2.27	2.31	2.35	2.32	2.45
Getis-Ord Gi z-score (cold spot)	Min	−5.51	−5.65	−5.60	−5.17	−7.01
	Max	−1.96	−1.98	−1.97	−1.97	−1.98
	Mean	−2.72	−2.69	−2.70	−2.68	−3.10
Getis-Ord General G	Observed general G	0.003	0.003	0.003	0.003	0.005
	z-score	5.08	5.03	4.79	4.63	2.94
	p-value	0.00	0.00	0.00	0.00	0.00

occurs in summer.<sup>(33)</sup> Thus, the LSTs of the solar panels are slightly higher than  $LST_p$  in the video mosaics. Simultaneously, the video mosaics show larger differences in the spatial distributions in both the hot and cold spots for longer frame intervals (Table 3). In the video mosaics, the longer the time frame interval, the more heterogeneous the spatial patterns are compared with those obtained from the photomosaics.

Figure 4 displays the spatial patterns of clusters that are classified with 1.5 °C LST intervals. Traditionally, clusters are classified with respect to the values used to inspect the inherent characteristics of the data set. Thus, when applying a traditional clustering method, such as the hierarchical clustering,  $k$ -means, clustering large applications, or Ward algorithm,<sup>(34,35)</sup> the standard for classifying a cluster is deduced in accordance with the LST. These standards preclude a subjective comparison of the spatial distributions of clusters between  $LST_p$  versus  $LST_{15frames}$ ,  $LST_{7.5frames}$ ,  $LST_{1frame}$ , and  $LST_{0.5frame}$ . Accordingly, we utilize equal intervals and divide the sums of the minimum and maximum  $LST_p$  values by five to classify five clusters with similar intervals as  $LST_{15frames}$ ,  $LST_{7.5frames}$ ,  $LST_{1frame}$ , and  $LST_{0.5frame}$ .

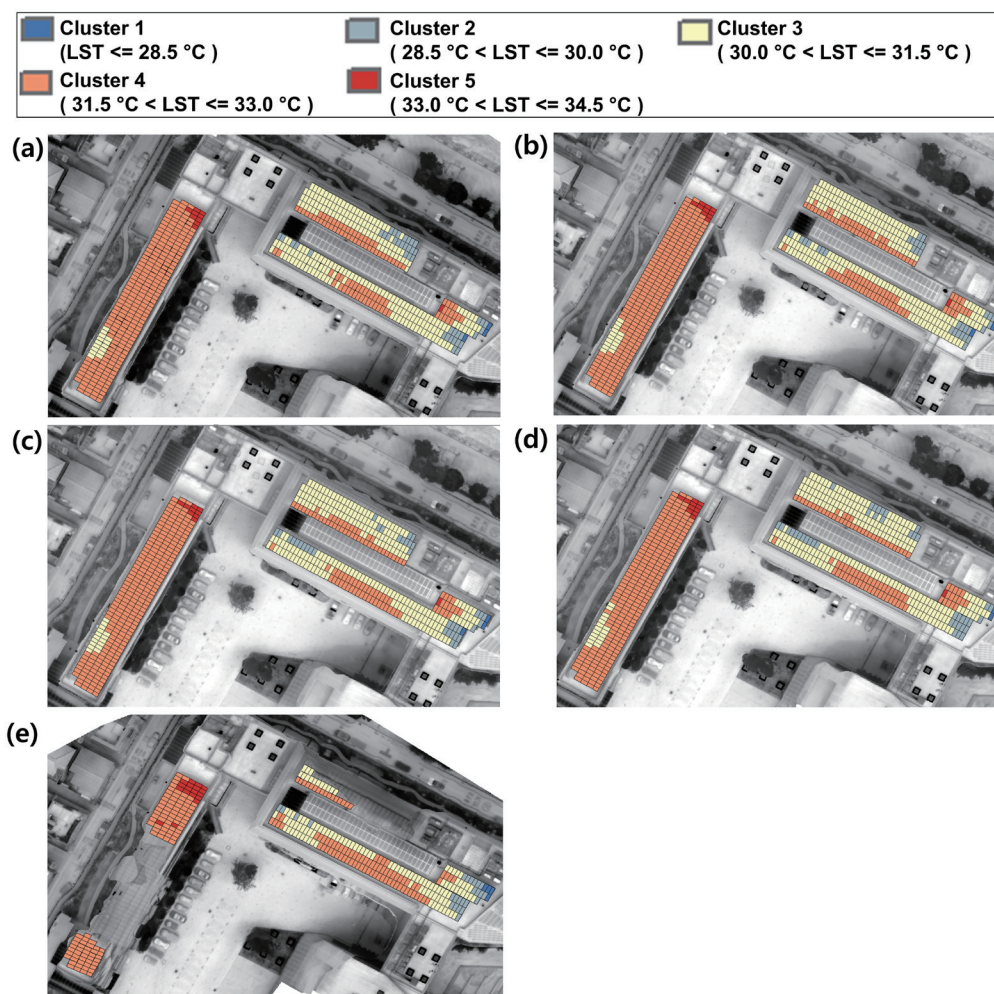


Fig. 4. (Color online) Distribution map of solar panel clusters based on LSTs of solar panels: (a) photomosaic, (b) 15, (c) 7.5, (d) 1, and (e) 0.5 frame/s.

Table 4 presents the results of the cluster analysis; the numbers of solar panels in the classified clusters and the similarity in the spatial location between photo- and video mosaics are also indicated. This similarity is calculated on the basis of the number of matched solar panels being classified as the same cluster in both the photo- and video mosaics. In all video mosaics processed with  $LST_{15frames}$ ,  $LST_{7.5frames}$ , and  $LST_{1frame}$ , the spatial patterns of clusters from the video mosaics are similar to those in the photomosaic. The similarity of spatial patterns of clusters to  $LST_p$  appears to be high in the video mosaics with  $LST_{15frames}$ ,  $LST_{7.5frames}$ , and  $LST_{1frame}$ .  $LST_{0.5frame}$  has the lowest similarity of spatial patterns of clusters to  $LST_p$  in most clusters (38.4–66.7%), except for Cluster 5 (90.0%) (Table 3). From 13:00 to 14:00, the difference in LSTs is under 1 °C.<sup>(36)</sup> However, the differences between  $LST_p$  and  $LST_{0.5frame}$  range from –0.86 to 1.45 °C (Table 5). The differences are excessive for  $LST_{0.5frame}$  even when considering the time lag during shooting.

The UAV images have radially decreasing brightness away from the center.<sup>(37)</sup> This is termed the vignetting effect, which is caused by optical transmission problems.<sup>(38)</sup> The spatial transmissivity of an image with vignetting is normalized to a maximum value of 1. Typically, a

Table 4

Results of comparative evaluations of similarity of spatial patterns regarding solar panel LSTs. Similarity is calculated by dividing the total number of solar panels in specific clusters detected via the photomosaic by the spatially matched number of solar panels in the respective clusters for photo- and video mosaics.

Frame intervals		Photomosaic	15 frames/s	7.5 frames/s	1 frame/s	0.5 frame/s
Number of solar panels		645	645	645	645	359
Number of solar panels in individual clusters	Cluster 1	3	3	3	2	4
	Cluster 2	40	36	37	42	25
	Cluster 3	242	240	242	244	114
	Cluster 4	350	355	353	345	198
	Cluster 5	10	11	10	12	18
Similarity in cluster spatial location between photo- and video mosaics (%)	Cluster 1	—	100	100	66.7	66.7
	Cluster 2	—	80.0	77.5	65.0	40.0
	Cluster 3	—	93.4	94.2	89.3	38.4
	Cluster 4	—	97.7	98.3	95.4	45.7
	Cluster 5	—	90.0	90.0	100.0	90.0

Table 5

Differences in LSTs between photo- and video mosaics. The differences are calculated by subtracting LSTs of the solar panels detected from video stream from  $LST_p$ . Negative (–) differences denote that LSTs detected from video mosaics are overestimated relative to  $LST_p$ .

Frame interval		$LST_{15frames}$	$LST_{7.5frames}$	$LST_{1frame}$	$LST_{0.5frame}$
Number of solar panels	Negative (–) differences	287	293	323	268
	Positive (+) differences	358	352	322	91
Difference (°C)	Min	–0.326	–0.366	–0.604	–0.855
	Max	0.412	0.310	0.563	1.446
	Mean	0.001	0.007	–0.005	–0.106
	Sum	0.951	4.357	–3.283	–38.02
	S.D.	0.13	0.14	0.21	0.52

Table 6

Results of comparative evaluation of point cloud between the video- and photomosaics.

Frame interval	Photomosaic	15 frames/s	7.5 frames/s	1 frame/s	0.5 frame/s
Overlapping rate	95	99	99	97	88
3D densified keypoints (m <sup>3</sup> )	5.3	21.36	21.10	15.76	13.28

camera captures more light in the center of an image than at its borders. Thus, the transmissivity of an image is 1 in the center and decreases toward the borders. In Pix4dMapper, a vignetting polynomial is applied by modeling the camera optics using the coefficients included in image headers to correct the vignetting effect.<sup>(39,40)</sup> During mosaicking, the matched points among the images are calculated using the mean values of the matched keypoints. Thus, similar results to those when the image edges are excluded can be obtained.<sup>(41)</sup> The lower the image overlapping rate, the smaller the number of matched keypoints deduced. Insufficient keypoints lead to biased results, including the vignetting effect. This tendency is clearly apparent in the results of this study: longer frame intervals (15→7.5→1→0.5 frame/s) have lower overlapping rates (99→99→97→88%) and fewer 3D densified keypoints per cubic meter (21.36→21.10→15.76→13.28 per m<sup>3</sup>) (Table 6). Hence, the low similarity of spatial patterns of clusters to  $LST_p$  in  $LST_{0.5frame}$  might be due to the lack of keypoints and the vignetting effect caused by the low overlapping rate (88%).

The frame interval is strongly associated with the overlapping rate. When the frame interval increased from 15 to 0.5 frame/s, the overlapping rate decreased from 99 to 88%. The video mosaics built with the longer video frame intervals have a lower similarity to the photomosaic. Therefore, video mosaics can be used to inspect the spatial patterns of defective inner-city solar panels with a similar overlapping rate to that of photomosaics. However, we observed that a video mosaic with a lower frame interval than the photomosaic reduced the number of 3D densified keypoints per cubic meter. An insufficient number of keypoints leads to the generation of biased thermal signatures and exterior orientation parameters (distances, angles, positions, and areas of solar panels). Therefore, video thermal photomosaics must have frame intervals that match or exceed the overlapping rates achieved with autopilot to ensure the consistent quality of thermal signatures obtained from video mosaics and photomosaics.

The development stages for UAV autopilot can be divided as follows: (1) Level 0: Non-automated, (2) Level 1: Automated assistance (3), Level 2: Monitored automation (4), Level 3: Conditional automation, (5) Level 4: Full automation.<sup>(6)</sup> The UAV autopilot used in this study was judged to correspond to Level 1 because the route flight was performed with each waypoint manually entered by the human pilot. Most of the solar panel monitoring using a UAV in this study depends on Level 1 technology.<sup>(42)</sup> In the full automation stage (Level 4), the autopilot allows the UAV to reach the desired destination without human intervention while recognizing and avoiding obstacles through its sensor. Therefore, it is judged that the problems raised in this study can be solved if technological development in the full automation stage (Level 4) is achieved in connection with the video sensor.

## 4. Conclusions

To our knowledge, this is the first study of comparing the capabilities of tracking spatial patterns on defective urban solar panels between UAV video mosaics and autopilot-based photomosaics. We experimentally validated the spatial distribution of hot spots. Clusters of thermal signatures in video mosaics have the highest similarity (80–100%) to those in the photomosaic while providing higher frame intervals (15 frames/s). Even when a video mosaic is obtained with a shorter flight duration and smaller coverage area than a photomosaic, it can achieve the required performance in tracking thermal deficiency on targeted urban solar panels. The results of this study can serve as preliminary evidence for the applicability of video-based thermal imaging to thermal deficiency inspection on urban solar panels.

## Acknowledgments

This research was supported by the Basic Science Research Program through the National Research Foundation of Korea (NRF) funded by the Ministry of Education (2021R1A6A3A01087241). It was also supported by a National Research Foundation of Korea (NRF) grant funded by the Korean government (MSIT, NRF-2021R1F1A1051827).

## References

- 1 Y. Zefri, A. ElKettani, I. Sebari, and S. Ait Lamallam: *Drones* **2** (2018) 41. <https://doi.org/10.3390/drones2040041>
- 2 Y.-S. Hwang, S. Schlüter, S.-I. Park, and J.-S. Um: *Remote Sens.* **14** (2022) 1220. <https://doi.org/10.3390/rs14051220>
- 3 D. H. Lee and J. H. Park: *Energies* **12** (2019) 2928. <https://doi.org/10.3390/en12152928>
- 4 P. Zhang, L. Zhang, T. Wu, H. Zhang, and X. Sun: *J. Appl. Remote Sens.* **11** (2017) 016026. <https://doi.org/10.1117/1.JRS.11.016026>
- 5 Y.-S. Hwang, S. Schlüter, S.-I. Park, and J.-S. Um: *Remote Sens.* **13** (2021) 2745. <https://doi.org/10.3390/rs13142745>
- 6 J.-S. Um: *Drones as Cyber-Physical Systems* (Springer, Singapore, 2019). <https://doi.org/10.1007/978-981-13-3741-3>
- 7 Y. Yao and Y. Hu: 2017 2nd Asia-Pacific Conference on Intelligent Robot Systems (ACIRS) (2017) 7. <https://doi.org/10.1109/ACIRS.2017.7986055>
- 8 T. Jurca, E. Tulcan-Paulescu, C. Dughir, M. Lascu, P. Gravila, A. D. Sabata, I. Luminosu, C. D. Sabata, and M. Paulescu: *AIP Conf. Proc.* **1387** (2011) 253. <https://doi.org/10.1063/1.3647083>
- 9 J.-S. Um and R. Wright: *Geocarto Int.* **14** (1999) 24. <https://doi.org/10.1080/10106049908542090>
- 10 J.-S. Um and R. Wright: *Sci. Total Environ.* **215** (1998) 189. [https://doi.org/10.1016/S0048-9697\(97\)00340-9](https://doi.org/10.1016/S0048-9697(97)00340-9)
- 11 J.-S. Um and R. Wright: *Int. J. Remote Sens.* **20** (1999) 2015. <https://doi.org/10.1080/014311699212326>
- 12 H. V. Nguyen and L. H. Tran: 20th Int. Conf. Methods and Models in Automation and Robotics (MMAR) (2015) 829. <https://doi.org/10.1109/MMAR.2015.7283983>
- 13 F. S. Leira, T. A. Johansen, and T. I. Fossen: 2015 IEEE Aerospace Conf. (2015) 1. <https://doi.org/10.1109/AERO.2015.7119238>
- 14 J. Kwon, Y. Kim, and S. H. Choi: *Spat. Inf. Res.* **27** (2019) 87. <https://doi.org/10.1007/s41324-018-0205-z>
- 15 D. Gómez-Candón, N. Virlet, S. Labbé, A. Jolivot, and J.-L. Regnard: *Precis. Agric.* **17** (2016) 786. <https://doi.org/10.1007/s11119-016-9449-6>
- 16 C. Yuan, Z. Liu, and Y. Zhang: 2015 Int. Conf. Unmanned Aircraft Systems (ICUAS) (2015) 639. <https://doi.org/10.1109/ICUAS.2015.7152345>
- 17 S. Lafkih and Y. Zaz: 2017 Int. Renewable and Sustainable Energy Conf. (IRSEC) (2017). <https://doi.org/10.1109/IRSEC.2017.8477387>

- 18 L. López-Fernández, S. Lagüela, J. Fernández, and D. González-Aguilera: Remote Sens. **9** (2017) 631. <https://doi.org/10.3390/rs9060631>
- 19 Y.-S. Hwang, S. Schlüter, J.-J. Lee, and J.-S. Um: Remote Sens. **13** (2021) 4770. <https://doi.org/10.3390/rs13234770>
- 20 S.-I. Park, T.-H. Ryu, I.-C. Choi, and J.-S. Um: Energies **12** (2019) 2787. <https://doi.org/10.3390/en12142787>
- 21 Y. Hwang and J.-S. Um: Spat. Inf. Res. **25** (2017) 361. <https://doi.org/10.1007/s41324-017-0103-9>
- 22 Y.-S. Hwang, J.-J. Lee, S.-I. Park, and J.-S. Um: Sens. Mater. **31** (2019) 3773. <https://doi.org/10.18494/SAM.2019.2522>
- 23 G. De Haan: Video Processing for Multimedia Systems (Citeseer, 2000). <https://citeseerx.ist.psu.edu/viewdoc/summary?doi=10.1.1.468.2159>
- 24 J.-J. Lee, Y.-S. Hwang, S.-I. Park, and J.-S. Um: J. Environ. Impact Assess **27** (2018) 475. <https://doi.org/https://doi.org/10.14249/eia.2018.27.5.475>
- 25 J.-S. Um: Spatial Inf. Res. **25** (2017) 585. <https://doi.org/10.1007/s41324-017-0126-2>
- 26 S.-I. Park, Y.-S. Hwang, J.-J. Lee, and J.-S. Um: J. Coast. **114** (2021) 474. <https://doi.org/10.2112/jcr-si114-096.1>
- 27 J.-S. Um: Spat. Inf. Res. **26** (2018) 143. <https://doi.org/10.1007/s41324-018-0163-5>
- 28 J.-S. Um: Spat. Inf. Res. **25** (2017) 439. <https://doi.org/10.1007/s41324-017-0112-8>
- 29 Y. Liu, X. Zheng, G. Ai, Y. Zhang, and Y. Zuo: ISPRS Int. J. Geoinf. **7** (2018) 333. <https://doi.org/10.3390/ijgi7090333>
- 30 R. T. Alberto, J. C. E. Rivera, A. R. Biagtan, and M. F. Isip: Spat. Inf. Res. **28** (2020) 383. <https://doi.org/10.1007/s41324-019-00302-z>
- 31 G. Khan, X. Qin, and D. A. Noyce: J. Transp. Eng. **134** (2008) 191. [https://doi.org/10.1061/\(ASCE\)0733-947X\(2008\)134:5\(191\)](https://doi.org/10.1061/(ASCE)0733-947X(2008)134:5(191))
- 32 A. Getis and K. Ord: Geogr. Anal. **24** (1992) 189. <https://doi.org/10.1111/j.1538-4632.1992.tb00261.x>
- 33 J. P. A. Martins, I. F. Trigo, N. Ghilain, C. Jimenez, F.-M. Götttsche, S. L. Ermida, F.-S. Olesen, F. Gellens-Meulenberghs, and A. Arboleda: Remote Sens. **11** (2019) 3044. <https://doi.org/10.3390/rs11243044>
- 34 Y. Hwang, J.-S. Um, and S. Schlüter: Int. J. Environ. Res. Public Health **17** (2020) 5976. <https://doi.org/10.3390/ijerph17165976>
- 35 M. Z. Rodriguez, C. H. Comin, D. Casanova, O. M. Bruno, D. R. Amancio, L. d. F. Costa, and F. A. Rodrigues: PLOS ONE **14** (2019) e0210236. <https://doi.org/10.1371/journal.pone.0210236>
- 36 L. Huang, J. Li, D. Zhao, and J. Zhu: Build. Environ. **43** (2008) 7. <https://doi.org/10.1016/j.buildenv.2006.11.025>
- 37 X. Yuan, X. Wang, A. Dou, and X. Ding: IGARSS 2018 - 2018 IEEE Int. Geoscience and Remote Sensing Symp. (2018) 5704. <https://doi.org/10.1109/IGARSS.2018.8517825>
- 38 A. Kordecki, H. Palus, and A. Bal: Signal Image Video Process. **10** (2016) 1417. <https://doi.org/10.1007/s11760-016-0941-2>
- 39 J. Kelly, N. Kljun, P.-O. Olsson, L. Mihai, B. Liljeblad, P. Weslien, L. Klemedtsson, and L. Eklundh: Remote Sens. **11** (2019) 567. <https://doi.org/10.3390/rs11050567>
- 40 Y.-H. Tu, S. Phinn, K. Johansen, and A. Robson: Remote Sens. **10** (2018) 1684. <https://doi.org/10.3390/rs10111684>
- 41 H. Hoffmann, H. Nieto, R. Jensen, R. Guzinski, P. Zarco-Tejada, and T. Friborg: Hydrol. Earth Syst. Sci. **20** (2016) 697. <https://doi.org/10.5194/hess-20-697-2016>
- 42 F. Al-Turjman and H. Zahmatkesh: In Unmanned Aerial Vehicles in Smart Cities (Springer International Publishing, Cham, 2020) p. 1. [https://doi.org/10.1007/978-3-030-38712-9\\_1](https://doi.org/10.1007/978-3-030-38712-9_1)